Qingyu Xiao
Department of Biomedical Engineering,
Georgia Institute of Technology,
Atlanta, GA 30332
e-mail: qxiao33@gatech.edu

Mishek Musa
Department of Mechanical Engineering,
University of Arkansas,
Fayetteville, AR 72701
e-mail: mjmusa@uark.edu

Isuru S. Godage
College of Computing and Digital Media,
DePaul University,
Chicago, IL 60604
e-mail: igodage@exchange.tamu.edu

Hao Su
Department of Mechanical
and Aerospace Engineering,
North Carolina State University,
Raleigh, NC 27695
e-mail: hsu4@ncsu.edu

Yue Chen[1]
Department of Biomedical Engineering,
Georgia Institute of Technology,
Atlanta, GA 30332
e-mail: yue.chen@bme.gatech.edu

Kinematics and Stiffness Modeling of Soft Robot With a Concentric Backbone

Soft robots can undergo large elastic deformations and adapt to complex shapes. However, they lack the structural strength to withstand external loads due to the intrinsic compliance of fabrication materials (silicone or rubber). In this paper, we present a novel stiffness modulation approach that controls the robot's stiffness on-demand without permanently affecting the intrinsic compliance of the elastomeric body. Inspired by concentric tube robots, this approach uses a Nitinol tube as the backbone, which can be slid in and out of the soft robot body to achieve robot pose or stiffness modulation. To validate the proposed idea, we fabricated a tendon-driven concentric tube (TDCT) soft robot and developed the model based on Cosserat rod theory. The model is validated in different scenarios by varying the joint-space tendon input and task-space external contact force. Experimental results indicate that the model is capable of estimating the shape of the TDCT soft robot with an average root-mean-square error (RMSE) of 0.90 (0.56% of total length) mm and average tip error of 1.49 (0.93% of total length) mm. Simulation studies demonstrate that the Nitinol backbone insertion can enhance the kinematic workspace and reduce the compliance of the TDCT soft robot by 57.7%. Two case studies (object manipulation and soft laparoscopic photodynamic therapy) are presented to demonstrate the potential application of the proposed design.
[DOI: 10.1115/1.4055860]

Keywords: soft robots, concentric tube robot, kinematics modeling, stiffness modulation

1 Introduction

Soft robots, fabricated from soft materials such as polymer or silicone, are designed to overcome the limitations of conventional rigid robotic systems in their inability to safely and effectively interact with real-world environments outside of a controlled setting [1,2]. For example, a rigid industrial robotic arm has to be placed within a safeguard during its operation. On the other hand, plants and animals, for example, have gone through natural evolution to develop intrinsically compliant mechanisms ideal for survival in a wide range of environments [3]. Designers of soft robots often take inspiration from these mechanisms and employ novel materials and techniques to create structures and actuators capable of large elastic deformations.

However, despite an impressive amount of research in soft robotics that establishes immense potential, they are yet to make applications outside laboratory settings. This is partially due to their lack of structural strength, necessary to exert force on the environment (i.e., manipulate objects and move payloads) while supporting their own weight [4]. Thus, stiffness modulation is often necessary to enhance the soft robot's mechanical strength to satisfy different application requirements. Low stiffness allows the robot to conform to the environment, while high stiffness is needed to transmit force or to bear loads. Literature reviews indicate that soft robot stiffness can be modulated via the thermal-based methods, magneto-rheological (MR)/electro-rheological (ER) based methods, jamming-based methods, and antagonistic-based methods [5,6].

Thermal-based methods are achieved by integrating the soft robots with the additive materials whose stiffness varies with respect to temperature. These additive materials include shape memory polymers [7–11], thermoplastics such as polylactic acid (PLA) or Acrylonitrile butadiene styrene (ABS) [6,12], low melting-point alloys [13–17], and others such as wax [18]. The primary limitation of thermal-based methods is that heating or cooling these materials requires additional sets of power electronics and sensory feedback systems. Moreover, they typically require a long response time (as large as 50 s [10]) due to the nature of heat dissipation, which may not be sufficient to achieve real-time stiffness control. MR/ER-based methods employ the MR or ER fluids that could change from soft to rigid state subject to an external magnetic field or electric field [19–21]. Soft robot stiffness can be readily modulated by controlling the strength of magnetic or electric field. However, ER-based methods require a high voltage source (1–5 kV [21]) to produce the required electric field, potentially imposing a safety hazard to humans. MR-based methods can achieve stiffness modulation in a low magnetic field (10–35 mT [19,20,22]), but they still require external electromagnets or permanent magnets to control the magnetic field strength [22]. Jamming-based methods typically rely on vacuums to depressurize the encapsulated particles and surface layers, leading to increased friction between particles [23–25] or surface layers [26–28], and hence increasing the stiffness of soft robotic manipulator. However, soft robots using these methods require additional channels to encapsulate particles, leading to increased dimensions of the robot itself (diameter around 45 mm [23,25]). Extra space is also needed for cumbersome pneumatic pumps, making them challenging to be applied in the confined operation space, such as the clinical operating room. Besides, the particles inside the channels have the risk of damaging the surrounding membranes or sheaths, and will exacerbate the hysteresis [29]. To use the antagonistic-based methods for stiffness

[1]Corresponding author.

Contributed by the Mechanisms and Robotics Committee of ASME for publication in the Journal of Mechanisms and Robotics. Manuscript received March 2, 2022; final manuscript received September 15, 2022; published online November 25, 2022. Assoc. Editor: Guangbo Hao.

modulation, soft robots are assembled with actuators that operate in the opposite direction [30–33]. The stiffness can be tuned by simultaneously actuating opposed actuators. But the robots with these methods are inefficient in that they require multiple actuators to finish a task which can be achieved by just one actuator from other aforementioned methods.

The aforementioned stiffness modulation methods have shown significant enhancement of soft robot stiffness but still have certain limitations such as prolonged response time and require for additional cumbersome power-electronic systems. Also, those methods typically increase the stiffness when the soft robot has reached the desired position. The stiffness is enhanced up to several orders of magnitude higher than the original stiffness, leading to a shape lock. This is beneficial to holding large loads but will lose the inherent dexterity and compliance of the soft robot. Therefore, the desire for a design that can achieve fast stiffness modulation and maintain the robot manipulability at the same time motivates the work in this paper. Inspired by the concentric tube robot, we propose a new method for soft robot stiffness modulation by adding a super-elastic Nitinol backbone to a tendon-driven soft robot. Concentric tube robot consists of a set of pre-curved, super-elastic tubes that are nested together [34,35]. Extending or rotating the inner tube with respect to the outer one leads to the variation of overall configuration and stiffness. Similar to the concentric tube robot, the tendon-driven soft robot is analogous to the outer tube, while the Nitinol backbone is analogous to the inner tube. The advantage of the proposed method can achieve fast stiffness modulation. Moreover, the soft robot can change the stiffness during the manipulation when the soft robot is moving. The proposed stiffness modulation method can be applied to a variety of soft robots, such as pneumatic-driven and hydraulic-driven soft robots. And this method can be achieved via electromechanical motors directly, which has a fast response and is hygienic for clinical use. Our new stiffness modulation idea was experimentally validated in a tendon-driven, concentric tube (TDCT) backbone soft robot. The motivation of evaluating it in a tendon-driven soft robot is to leverage the advantage of easy fabrication and simple joint-space control. The contribution of the proposed work includes:

(1) Proposed a new stiffness modulation concept and evaluated through a custom-designed TDCT soft robot.
(2) Developed and experimentally validated the mechanics modeling for the proposed TDCT soft robot.

The rest of this paper is organized as follows: Sec. 2 describes the design and modeling of the TDCT soft robot; Sec. 3 illustrates the experimental setups and validation results for the proposed modeling method; Sec. 4 performs simulation study of the TDCT soft robot kinematics and compliance; Sec. 5 presents two case studies of the TDCT soft robot; and Sec. 6 is the conclusion of this paper.

2 Design and Modeling

2.1 Design of TDCT Soft Robot. The proposed TDCT soft robot leverages the mechanical stiffness of Nitinol and the compliance of silicone to achieve desired soft robot stiffness modulation. The robot CAD model can be seen in Fig. 1. The soft robot consists of four narrow channels molded within its elastomeric body to enable easy control of robot bending in x or y directions. The elastomeric body of the soft robot is made of Elastosil M4601 A/B (Wacker Chemie AG), and a Nitinol tube can slide in and out of the central channel to modulate the robot's configuration and stiffness. The Nylon tendons are routed straight and parallel to the backbone. Nitinol backbone can sustain large deformations without plastic deformations. Note that the Nitinol backbone is manually inserted into TDCT soft robot central channel in this preliminary study. However, it can be automatically inserted via a linear actuator to achieve real-time stiffness modulation. Also, the proposed idea can also be used for multi-segments soft robot [36].

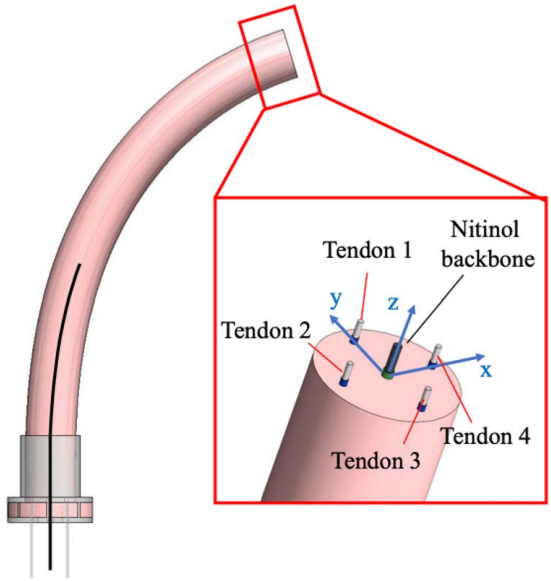

Fig. 1 Design of TDCT soft robot with a super-elastic retractable Nitinol tube (black curve) for stiffness modulation. Four tendons are symmetrically located at the cross section with the same distance to the center. The Nitinol insertion can be achieved manually (in this paper) or via precise linear motors. Noting that friction-reducing sleeves are integrated with the soft robot to reduce the friction between the soft robot and tendons/Nitinol tube.

2.2 Robot Mechanics Modeling. The configuration of the proposed TDCT soft robot is determined by the joint-space tensions provided by the inelastic tendon wire, joint-space Nitinol backbone insertion depth, and task-space external load. As shown in Fig. 2, the mechanics modeling of the TDCT soft robot can be carried out by considering the following two segments, which are pure silicone body actuated by tendon wires (segment 1) and soft silicone body with Nitinol backbone (segment 2). Segment 1 is a standard tendon-driven soft robot and has been extensively studied [37–39]. For example, the kinematics of tendon-driven robots can be developed based on the constant curvature assumption [37] or calibration-based method [40]. However, this modeling method may not be able to handle the complicated robot deformations due to various external loads. This motivates the development of generalized modeling such as finite element method [38] or Cosserat rod theory [39]. In this paper, we calculate kinematics/mechanics of segment 1 based on the method described in

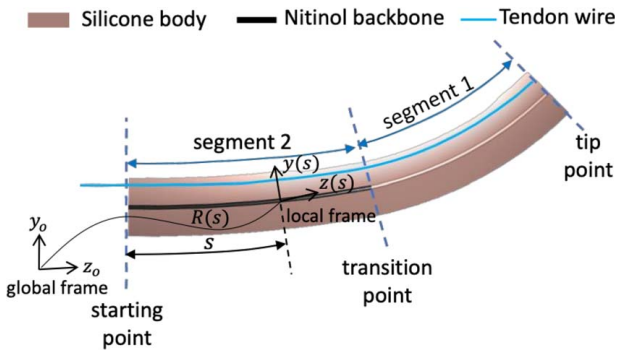

Fig. 2 The TDCT soft robot can be separated by the transition point. Segment 1 is the region without Nitinol backbone (assume that the Nitinol backbone insertion depth is less than the TDCT soft robot length), while segment 2 is the overlapped region of Nitinol backbone and silicone body.

Ref. [41], which can be written in (1):

$$\begin{aligned}\dot{\boldsymbol{p}} &= R\boldsymbol{v}\\ \dot{R} &= R\hat{\boldsymbol{u}}\\ \begin{bmatrix}\dot{\boldsymbol{v}}\\ \dot{\boldsymbol{u}}\end{bmatrix} &= \begin{bmatrix}k_{SE}+Q & G\\ T & k_{BT}+H\end{bmatrix}^{-1}\begin{bmatrix}\boldsymbol{d}\\ \boldsymbol{c}\end{bmatrix}\end{aligned} \tag{1}$$

where $\boldsymbol{p}$, R, $\boldsymbol{v}$, and $\boldsymbol{u}$ are defined in Table 1. Q, T, G, H, $\boldsymbol{d}$, and $\boldsymbol{c}$ are determined by the configuration space variables, external loads, and the tendon tensions as described in coupled rod and tendon model derived in Ref. [41] (see Table 1 for other detailed definition of each parameter).

Segment 2 is a tendon-drive soft robot with a Nitinol backbone. To create the mechanics model of segment 2, we take the following assumptions:

(1) The friction between the inner Nitinol backbone and outer soft robot, as well as the friction between tendon wire and outer soft robot, can be ignored. This can be achieved by embedding a friction-reducing sleeve to guide the backbone and tendon wires.
(2) The inner Nitinol backbone and the medial axis of the outer soft robot body are concentric, which can be satisfied via an accurate fabrication process.
(3) Shear strain of Nitinol backbone is negligible.

Based on these assumptions, the outer silicone body can be freely compressed, extended, or rotated along the local z direction and interacts with the inner Nitinol backbone when it is bending or shearing in local x and y axes, as illustrated in Fig. 2. This indicates that the force or moment of soft robot in local x and y directions can be lumped together, whereas the component in the z direction should be analyzed separately. Figure 3 illustrates the force analysis of segment 2 based on Cosserat rod theory, which can be written in the following equations:

$$\dot{\boldsymbol{n}}_1 = -\sum_{t=1}^{N_t}\boldsymbol{f}_t - \boldsymbol{f}_e - \boldsymbol{f}_c - \rho_1\boldsymbol{g} \tag{2}$$

$$\dot{\boldsymbol{n}}_2 = \boldsymbol{f}_c - \rho_2\boldsymbol{g} \tag{3}$$

Table 1 Notations in the mathematical model

Symbol	Unit	Definition
s	m	Arclength
ρ	kg/m	Linear density
$\dot{X}$	–	Derivative of X with respect to s
$\boldsymbol{r}$	m	Tendon position in the local frame
$\boldsymbol{p}$	m	Position with respect to origin
R	–	Rotation matrix from origin to $\boldsymbol{p}$
R_{ij}	–	The element of R in row i and column j
$\boldsymbol{n}$	N	Internal force in global frame
$\boldsymbol{m}$	N m	Internal moment in the global frame
$\boldsymbol{f}$	N	Distributed force in the global frame
$\boldsymbol{l}$	N m	Distributed moment in the global frame
$\boldsymbol{v}$	–	Rate of change of $\boldsymbol{p}$ to s
$\boldsymbol{u}$	1/m	Curvature vector in local frame
$\boldsymbol{v}^*$	–	$\boldsymbol{v}$ when robot is relaxed
$\boldsymbol{u}^*$	1/m	$\boldsymbol{u}$ when robot is relaxed
k_{SE}	N	Stiffness matrix for shear and extension
k_{BT}	N m^2	Stiffness matrix for bending and twisting
E	Pa	Young's modulus
G	Pa	Shear modulus
I	m^4	Second moment of area
A	m^2	Cross-sectional area
$(\hat{v})$	–	Skew-symmetric matrix of a vector $\boldsymbol{v}$
τ	N	Tension applied on the tendon
t	–	Subscription, representing the tth tendon
Q, G, T, H	–	Stiffness matrix defined in Ref. [41]

$$\dot{\boldsymbol{m}}_1 = -\dot{\boldsymbol{p}}_1\times\boldsymbol{n}_1 - \sum_{t=1}^{N_t}\boldsymbol{l}_t - \boldsymbol{l}_e - \boldsymbol{l}_c \tag{4}$$

$$\dot{\boldsymbol{m}}_2 = -\dot{\boldsymbol{p}}_2\times\boldsymbol{n}_2 + \boldsymbol{l}_c \tag{5}$$

where $\boldsymbol{n_1}$, $\boldsymbol{n_2}$, $\boldsymbol{m_1}$, and $\boldsymbol{m_2}$ are the internal forces and moments in the outer soft body and inner Nitinol backbone, respectively. The subscripts 1 and 2 in the above equations refer to the outer soft body and inner backbone, respectively. The terms $\boldsymbol{f_t}$ and $\boldsymbol{l_t}$ are the force and moment generated from the tth tendon wire to outer soft body defined in global frame, $\boldsymbol{f_e}$ and $\boldsymbol{l_e}$ are the force and moment from external load defined in the global frame, $\boldsymbol{f_c}$ and $\boldsymbol{l_c}$ are the interaction force and moment between the inner backbone and outer soft body in global frame, ρ_1 and ρ_2 are linear densities for soft body and Nitinol backbone, and $\boldsymbol{g}$ is the gravity vector in global frame. The corresponding positions of the soft body and backbone are indicated by $\boldsymbol{p_1}$ and $\boldsymbol{p_2}$. Taking the second modeling assumption into consideration, we have $\boldsymbol{p_1} = \boldsymbol{p_2}$ and $R_1 = R_2$. Hence, the internal forces and moments of both inner backbone and outer soft body can be lumped as in (6) and (7).

$$\dot{\boldsymbol{n}} = \dot{\boldsymbol{n}}_1 + \dot{\boldsymbol{n}}_2 = -\sum_{t=1}^{N_t}\boldsymbol{f}_t - \boldsymbol{f}_e - (\rho_1+\rho_2)\boldsymbol{g} \tag{6}$$

$$\dot{\boldsymbol{m}} = \dot{\boldsymbol{m}}_1 + \dot{\boldsymbol{m}}_2 = -\dot{\boldsymbol{p}}\times\boldsymbol{n} - \sum_{t=1}^{N_t}\boldsymbol{l}_t - \boldsymbol{l}_e \tag{7}$$

where $\boldsymbol{n}$ and $\boldsymbol{m}$ are the lumped internal force and moment. Note that the outer soft body can axially rotate with respect to the inner backbone due to the non-friction modeling assumption, and the linear constitutive relation is adopted and described as

$$\boldsymbol{n}_{x,y} = \boldsymbol{R}(\boldsymbol{k}_{SE,1}+\boldsymbol{k}_{SE,2})(\boldsymbol{v}-\boldsymbol{v}^*)|_{x,y} \tag{8}$$

$$\boldsymbol{n}_z = \boldsymbol{R}\boldsymbol{k}_{SE,1}(\boldsymbol{v}-\boldsymbol{v}^*)|_z \tag{9}$$

$$\boldsymbol{m}_{x,y} = \boldsymbol{R}(\boldsymbol{k}_{BT,1}+\boldsymbol{k}_{BT,2})(\boldsymbol{u}-\boldsymbol{u}^*)|_{x,y} \tag{10}$$

$$\boldsymbol{m}_z = \boldsymbol{R}\boldsymbol{k}_{BT,1}(\boldsymbol{u}-\boldsymbol{u}^*)|_z \tag{11}$$

where the stiffness matrices are $k_{SE} = \mathrm{diag}(k_{SE}^x\ k_{SE}^y\ k_{SE}^z)$ and $k_{BT} = \mathrm{diag}(k_{BT}^x\ k_{BT}^y\ k_{BT}^z)$. Other notations used in the above equations are defined in Table 1. Combining the linear constitutive relationship described in (8)–(11), we have the following equations:

$$\boldsymbol{n} = \begin{bmatrix}\boldsymbol{n}_x\\ \boldsymbol{n}_y\\ \boldsymbol{n}_z\end{bmatrix} = \boldsymbol{R}\boldsymbol{k}_{SE}(\boldsymbol{v}-\boldsymbol{v}^*) \tag{12}$$

$$\boldsymbol{m} = \begin{bmatrix}\boldsymbol{m}_x\\ \boldsymbol{m}_y\\ \boldsymbol{m}_z\end{bmatrix} = \boldsymbol{R}\boldsymbol{k}_{BT}(\boldsymbol{u}-\boldsymbol{u}^*) \tag{13}$$

where

$$k_{SE} = \mathrm{diag}(k_{SE1}^x + k_{SE2}^x\ k_{SE1}^y + k_{SE2}^y\ k_{SE1}^z) \tag{14}$$

$$k_{BT} = \mathrm{diag}(k_{BT1}^x + k_{BT2}^x\ k_{BT1}^y + k_{BT2}^y\ k_{BT1}^z) \tag{15}$$

where (14) and (15) indicate that we can consider the TDCT soft robot as a new soft robot which has the enhanced stiffness in local x and y directions, but the stiffness in local z direction remains unchanged. This forms our basic concept for stiffness modulation.

Note that the stiffness of Nitinol tube k_{SE2} is significantly larger than k_{SE1}, which leads to unobservable shear strain (deformation at

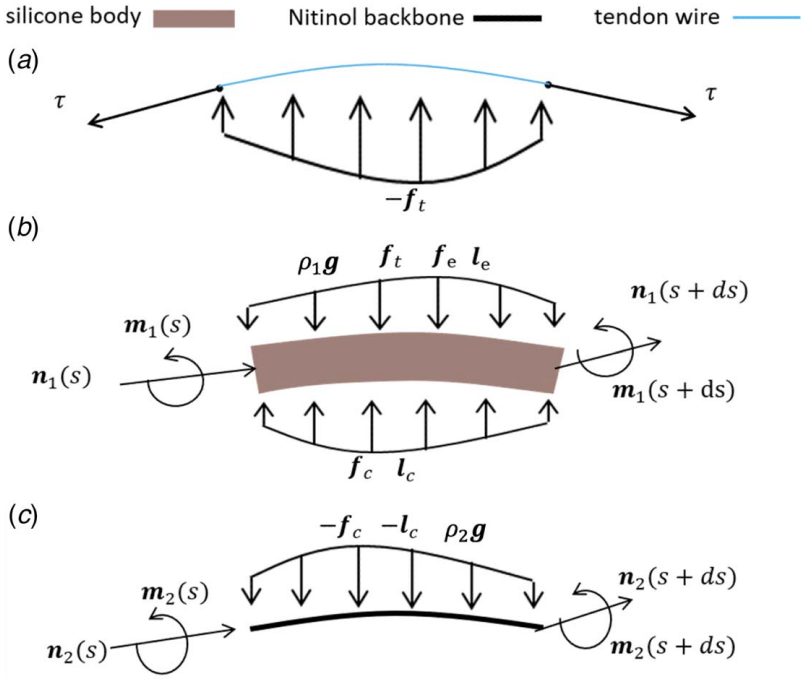

Fig. 3 Force analysis of segment 2 based on Cosserat rod theory: (*a*) The tendon wire is subjected to internal tension τ_t and reaction force $-f_t$ from silicone body, (*b*) Silicone body is subjected to interaction forces and moments from tendon wires f_t, Nitinol backbone (f_c and l_c), internal forces n_1 and moments m_1, ρ_1 and ρ_2 are linear density, and external loads f_e and moments l_e, and (c) Nitinol backbone is subjected to reaction forces $-f_c$ and moments $-l_c$ and internal forces n_2 and moments m_2.

x and y directions) due to the internal force n. However, the stiff backbone will not affect the compression or elongation (deformation at z direction) of the soft body because it can be freely inserted and pulled out. Therefore, the shear strain components (first and second elements) of v can be approximated to zeros and we only need to compute $\boldsymbol{v}$ at z direction, which is described in (16) and (17)

$$\boldsymbol{v} = [\boldsymbol{0}, \boldsymbol{0}, v_z]^T \tag{16}$$

$$v_z = 1 + [R_{31}\ R_{32}R_{33}]\boldsymbol{n}/(k^z_{SE1}) \tag{17}$$

And the derivative of the position and orientation can be computed by the rotation matrix times the local frame twist, and thus the soft robot pose can be obtained through the integration of (18) and (19)

$$\dot{\boldsymbol{p}} = R\boldsymbol{v} \tag{18}$$

$$\dot{R} = R\hat{\boldsymbol{u}} \tag{19}$$

Referring to Ref. [41], the tendon forces can be modeled in (20) if the friction between the TDCT soft robot and the tendons wire is negligible (see our modeling Assumption 1):

$$\boldsymbol{f}_t = \frac{\partial\left(\tau_t(\dot{\boldsymbol{p}}_t/\|\dot{\boldsymbol{p}}_t\|)\right)}{\partial s} \tag{20}$$

where $\boldsymbol{p}_t$ is the position of the tth tendon, $\boldsymbol{f}_t$ is the tth tendon force applied on the soft robot, and τ_t is the tth tension. Combining (16), (18), (19), and (20), tendon force can be simplified as (21)

$$\boldsymbol{f}_t = \tau_t R\hat{\boldsymbol{u}}[0\ 0\ 1]^T \tag{21}$$

Note that the above equation is obtained by assuming that $\dot{\boldsymbol{p}}_t \approx \dot{\boldsymbol{p}}$, which is true for a soft robot whose tendon wire is close to its backbone and is routed straight and parallel to the backbone. Hence the moment $\boldsymbol{l}_t$ acting on the soft robot by tendon can be computed by (22)

$$\boldsymbol{l}_t = (R\boldsymbol{r}_t)\times\boldsymbol{f}_t = \tau_t R\hat{\boldsymbol{r}}_t\hat{\boldsymbol{u}}[0\ 0\ 1]^T \tag{22}$$

where r_t is the coordinate of the tth tendon in the body frame. Combining the tendon force and moment in (21) and (22) with lumped model (6) and (7), and the concentric soft robot constitutive laws (16) and (17) with the shape model (18) and (19), we can obtain the proposed TDCT soft robot model, which can be re-organized as (23)–(26)

$$\dot{\boldsymbol{p}} = R[0\ 0\ v_z]^T \tag{23}$$

$$\dot{R} = R\hat{\boldsymbol{u}} \tag{24}$$

$$\dot{\boldsymbol{n}} = -\sum_{t=1}^{N_t}\tau_t R\hat{\boldsymbol{u}}[0\ 0\ 1]^T - (\rho_1+\rho_2)\boldsymbol{g} - \boldsymbol{f}_e \tag{25}$$

$$\dot{\boldsymbol{m}} = -\dot{\boldsymbol{p}}\times\boldsymbol{n} - \sum_{t=1}^{N_t}\tau_t R\hat{\boldsymbol{r}}_t\hat{\boldsymbol{u}}[0\ 0\ 1]^T - \boldsymbol{l}_e \tag{26}$$

where

$$v_z = 1 + [R_{31}\ R_{32}\ R_{33}]\boldsymbol{n}/(k^z_{SE1}) \tag{27}$$

$$\boldsymbol{u} = k_{BT}^{-1}R^T\boldsymbol{m} \tag{28}$$

$$k^z_{SE1} = E_1A_1 \tag{29}$$

$$k_{BT} = \begin{bmatrix} E_1 I_{1x} + E_2 I_{2x} & 0 & 0 \\ 0 & E_1 I_{1y} + E_2 I_{2y} & 0 \\ 0 & 0 & G_1 I_{1z} \end{bmatrix} \tag{30}$$

Note that the proposed model is used to calculate the pose of the TDCT soft robot where the Nitinol backbone and the silicone body are overlapped (see Fig. 2). If the Nitinol backbone insertion depth is smaller than TDCT soft robot length, the robot will have a transition point, after which the TDCT soft robot can be calculated based on Eq. (1).

2.3 Boundary Conditions. The proposed TDCT soft robot kinematics/mechanics is divided into two segments (see in Fig. 2), where segment 1 is similar to the conventional tendon-driven soft robot, and segment 2 is the overlapped region of the Nitinol backbone and the silicone body. Since the two segments of the TDCT soft robot are modeled by different methods, boundary conditions have to be considered to solve the modeling.

Notice that the variables of integration of segment 1 are $\boldsymbol{p}$, R, $\boldsymbol{v}$, and $\boldsymbol{u}$, whereas the integration of segment 2 relies on $\boldsymbol{p}$, R, $\boldsymbol{n}$, and $\boldsymbol{m}$ (see Eqs. (23)–(26)). Therefore, the conversions of these variables are necessary at the transition point to obtain the complete configuration of the TDCT soft robot. Force and moment analysis at the transition point indicates that the conservation law should be maintained, which gives

$$\boldsymbol{n}_1(L_{ni}) = \boldsymbol{n}(L_{ni}) \tag{31}$$

$$\boldsymbol{m}_1(L_{ni}) = \boldsymbol{m}(L_{ni}) \tag{32}$$

where L_{ni} refers to Nitinol backbone insertion depth. Using the constitutive relation in (12) and (13), the transition from a concentric soft robot model to a standard tendon-driven model is achieved by

$$\boldsymbol{p}_1(L_{ni}) = \boldsymbol{p}(L_{ni}) \tag{33}$$

$$R_1(L_{ni}) = R(L_{ni}) \tag{34}$$

$$\boldsymbol{v}_1(L_{ni}) = k_{SE1}^{-1} R^T(L_{ni}) \boldsymbol{n}(L_{ni}) + [0\ 0\ 1]^T \tag{35}$$

$$\boldsymbol{u}_1(L_{ni}) = k_{BT1}^{-1} R^T(L_{ni}) \boldsymbol{m}(L_{ni}) \tag{36}$$

The left-hand-side in (33)–(36) can be fed into the tendon-driven soft robot model to continue the shape calculation after transition point.

The boundary condition at the TDCT soft robot end effector ($s = L$) should also follow the conservation of force and moments as described in (37) and (38), respectively.

$$\boldsymbol{n}_2(L) + \sum_{t=1}^{N_t} \tau_t \frac{\dot{\boldsymbol{p}}}{\|\dot{\boldsymbol{p}}\|} + \boldsymbol{f}_e = \boldsymbol{0} \tag{37}$$

$$\boldsymbol{m}_2(L) + \sum_{t=1}^{N_t} \tau_t (\hat{R}\boldsymbol{r}_t) \frac{\dot{\boldsymbol{p}}}{\|\dot{\boldsymbol{p}}\|} + \boldsymbol{l}_e = \boldsymbol{0} \tag{38}$$

Shooting method is applied to solve the boundary value problem by converting it to an initial value optimization problem. The reason for adopting the shooting method to solve our model is that it has been proven to be a powerful method for solving many similar problems, such as tendon-driven continuum robot [42], concentric tube robot [43], and multi-backbone continuum robot [44]. In future work, we will also explore the efficiency of solving the differential equations with shooting methods and many other approaches [45]. The goal of the shooting method is to find the correct initial value of $\boldsymbol{n}(0)$ and $\boldsymbol{m}(0)$ such that they satisfy the boundary conditions in (37) and (38). Both the Euler method and the Runge–Kutta schemes can be used for the integration of the proposed ordinary differential equations. However, we choose the fourth-order Runge–Kutta scheme in this study to maintain accuracy and calculation stability. We use the function *fsolve* provided by MATLAB with default *Trust-Region-Dogleg Algorithm* to find the solution. Note that explicit numerical integration using Euler or Runge–Kutta schemes will cause numerical error in R defined in $SO(3)$. However, this error can be trivial for short integration arc lengths and relatively low curvatures that most continuum robot designs exhibit [46].

3 Experimental Validation of TDCT Soft Robot Modeling

In this section, we will implement the proposed mechanics model in MATLAB and validated it experimentally by considering various joint-space inputs and external loads. The soft robot gravity is also considered in the experimental validations. The runtime for solving the model is 0.82 ± 0.04 s using a laptop with CPU 2.3 GHz 8-core Intel Core i9. However, solving the model in real time can be achieved given Jacobian matrix computed in Ref. [47]. In our preliminary validation, we do not integrate high-speed computation algorithm to the solver.

3.1 Experimental Setup and Procedures. As shown in Fig. 4, the TDCT soft robot is mounted horizontally on an optical table. The actuation tendon is attached to a force sensor (Go Direct®, Vernier Inc., OR), which is connected to a lead screw mechanism. The TDCT soft robot is actuated by pulling the tendon wire via a stepper motor, and the corresponding tendon tension can be measured through the force sensor. External loads are achieved by attaching a weight at the distal tip of the TDCT soft robot. The Nitinol backbone is manually inserted with the depth measured by digital caliper. The shape of the TDCT soft robot is measured by a Φ1 mm fiber Bragg grating (FBG) sensor (FBGS International, Belgium). The shape data are reconstructed by *Shape Sensing v1.3.1* developed by FBGS International, which converts the wavelength variation to the positions of the fiber along its arclength.

To further verify our model of predicting the shape of the TDCT soft robot, we conducted experiments with multiple tendons actuated and applying loads that are not aligned with the bending plane. As the experimental setup presented in Fig. 5, the TDCT soft robot was actuated by the weights hanging on one or two of the tendons. External load at the tip is measured by ATI force sensor (ATI Industrial Automation, USA) mounted on the Franka Emika Panda robot (Franka Emika, German). The magnitude and the direction of the external load were computed by the forward kinematics of the robot arm and the three-directional force vector read from the ATI force sensor. The shape of the TDCT soft

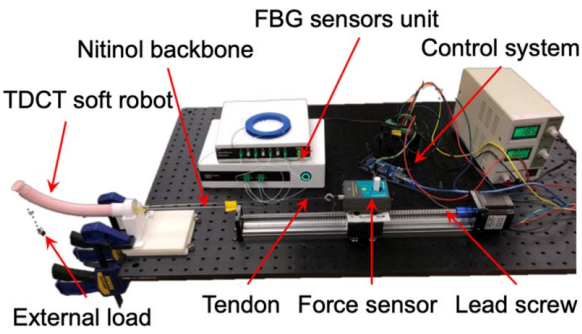

Fig. 4 Experimental setup for mechanics model validation with single tendon actuated and applying loads that align with the bending plane. The FBG sensor unit is used to acquire shape data.

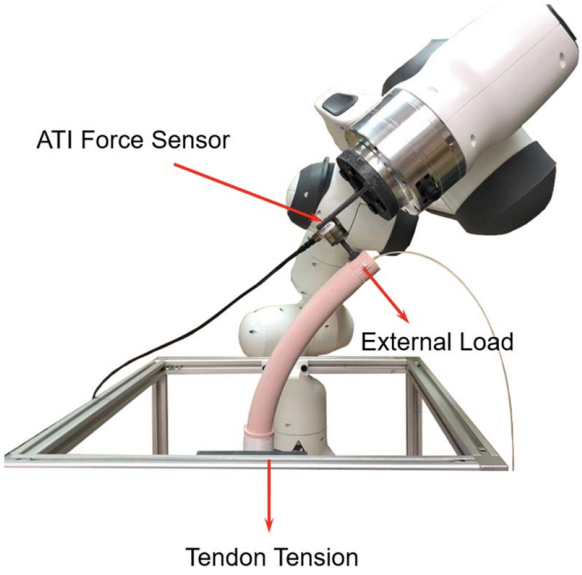

Fig. 5 Experimental setup for mechanics model validation with multiple tendons actuated and applying loads that not align with the bending plane

robot was acquired by the FBG sensor the same as the first experimental setup.

3.2 Mechanics Model Validation. The TDCT soft robot material properties are calibrated before the experimental validations. For the soft body of the TDCT soft robot, Young's modulus was experimentally calibrated. The TDCT soft robot was actuated by five distinct tendon forces on the same tendon. In all the five actuations, Nitinol tube was not inserted and no external load was applied at the tip. The Young's modulus, therefore, was calibrated by minimizing the error between the five experimental shapes and the corresponding modeling shapes. The shear modulus can be calculated by Young's modulus and Poisson's ratio. For the Nitinol tube, the Young's modulus of Nitinol tube is 83 GPa, which is obtained from the material certification. More parameters used for calculation in the mechanics model are presented in Table 2. The root-mean-squared error (RMSE) and tip error are used to evaluate the accuracy of the proposed model. The RMSE can be calculated by

$$\text{RMSE} = \sqrt{\frac{1}{N_p}\sum_{k=1}^{N_p} \|\boldsymbol{p}(s_k) - \boldsymbol{p}_{\exp}(s_k)\|^2} \tag{39}$$

where N_p is the total number of points of a shape, $\boldsymbol{p}(s_k)$ is the position of the modeling shape at the arc length s_k, and $\boldsymbol{p}_{\exp}(s_k)$ is the position of the experimental shape at the arc length s_k. The corresponding percentage of error with respect to the total length of the robot (L) is also computed.

Table 2 Parameters in the mechanics model

Outer diameters of Nitinol tube	1.397 mm
Inner diameters of Nitinol tube	1.118 mm
Outer diameter of soft robot	20 mm
Diameter of Nitinol tube insertion channel	1.5 mm
Young's modulus of soft robot	0.85 MPa
Young's modulus of Nitinol tube	83 GPa
Poisson ratio of soft robot	0.5
Poisson ratio of Nitinol	0.33
Soft robot length	160 mm

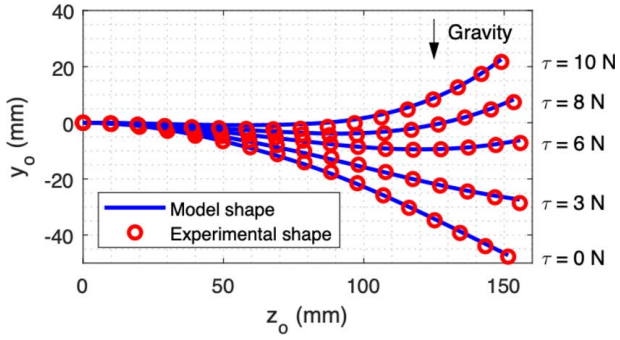

Fig. 6 Comparison of the modeling and experimental shape of the TDCT soft robot

In the first experiment, we tested our model with single tendon actuated and applying loads that align with the bending plane. This will evaluate the accuracy of our model for the TDCT soft robot in planar deformations. Figure 6 shows the modeling and experimental shapes of the TDCT soft robot obtained with the 20 g tip load, 80 mm Nitinol backbone, and various tensions, which indicate that the proposed model could accurately predict the TDCT soft robot shape. To further validate the accuracy of the proposed work, we tested our model under different combinations of tendon tensions (0 N, 3 N, 6 N, 8 N, and 10 N), inserted lengths of Nitinol (0 mm, 40 mm, 80 mm, and 120 mm), and the weights (0 g, 20 g, and 50 g) attached to the distal tip. This will produce the deformed robot with bending angle in the range of [−57.1 deg, + 61.4 deg]. The RMSE and tip error for each test are shown in Table 3 and results indicate that the proposed method can accurately predict the shape with the average RMSE of 0.75 mm (0.47% of total length) and the average tip error of 1.48 mm (0.92% of total length). And the maximum RMSE is 2.27 mm (1.42% of total length) and the maximum tip error is 3.46 mm (2.16% of total length). Notice that the RMSE becomes much larger with a larger tension or heavier weight. For tendon tensions of 0 N, 3 N, 6 N, 8 N, and 10 N, the average RMSEs are 0.45 mm, 0.51 mm, 0.74 mm, 0.95 mm, and 1.11 mm, respectively. And the tip errors are 1.36 mm, 1.33 mm, 1.34 mm, 1.64 mm, and 1.70 mm. This shows an increasing trend of RMSE and tip error when tendon tension becomes larger. This is potentially due to the nonlinear constitutive behavior of silicone occurring under these large deformation scenarios [48]. However, our proposed model achieved sufficient accuracy when the tension is less than 10 N and the weight is less than 50 g. Moreover, the RMSE and tip error decrease as the Nitinol insertion depth increases. For Nitinol insertion depth of 0 mm, 40 mm, 80 mm, and 120 mm, the average RMSEs are 1.00 mm, 0.74 mm, 0.72 mm, and 0.53 mm, respectively. The average tip errors are 1.75 mm, 1.48 mm, 1.47 mm, and 1.18 mm. This is potentially because the deformation becomes smaller as we insert the Nitinol tube, and hence the silicone has better linearity to satisfy the proposed model.

In the second experiment, we tested our model with multiple tendons actuated and applying loads that not align with the bending plane. Figure 7(*a*) presents the two results of TDCT soft robot actuated by single tendon with the same tension. The shape with black arrow at the tip is the result with external load applying at the tip. Similarly, Fig. 7(*b*) shows the two results of the TDCT soft robot actuated by two tendons with the same tendon tensions. Both figures show that with the experimental shape of the TDCT soft robot conforms to the model shape accurately with multiple tendons actuated and out-of-plane external load. To systematically evaluate the accuracy of the proposed work, we tested our model under different combinations of tendons, tendon tensions, inserted lengths of Nitinol, and the external load at distal tip. The RMSE result for each test is summarized in Table 4, showing that the proposed model can accurately predict the TDCT soft robot shape with

Table 3 Summary of single tendon actuation, in-plane external load experiment results

Case	Load (N)	Tendon (N)	RMSE (mm)				Tip error (mm)			
			$L=0$ mm	$L=40$ mm	$L=80$ mm	$L=120$ mm	$L=0$ mm	$L=40$ mm	$L=80$ mm	$L=120$ mm
1	0	0	0.81 (0.51%)	0.32 (0.20%)	0.19 (0.12%)	0.17 (0.11%)	1.64 (1.02%)	0.37 (0.23%)	1.18 (0.74%)	0.56 (0.35%)
2		3	0.51 (0.32%)	0.19 (0.12%)	0.35 (0.22%)	0.32 (0.20%)	0.89 (0.56%)	0.87 (0.54%)	1.23 (0.77%)	1.36 (0.85%)
3		6	0.53 (0.33%)	0.76 (0.47%)	0.58 (0.36%)	0.65 (0.41%)	0.64 (0.40%)	1.61 (1.01%)	0.61 (0.38%)	1.20 (0.75%)
4		8	0.77 (0.48%)	0.97 (0.61%)	0.83 (0.52%)	0.70 (0.44%)	1.66 (1.04%)	1.32 (0.83%)	2.09 (1.31%)	1.51 (0.94%)
5		10	1.16 (0.72%)	1.17 (0.73%)	1.11 (0.69%)	0.96 (0.60%)	2.58 (1.61%)	1.88 (1.18%)	1.28 (0.80%)	1.30 (0.81%)
6	0.20	0	0.58 (0.36%)	0.38 (0.24%)	0.46 (0.29%)	0.21 (0.13%)	1.46 (0.91%)	1.39 (0.87%)	1.72 (1.07%)	1.57 (0.98%)
7		3	0.50 (0.31%)	0.38 (0.24%)	0.44 (0.27%)	0.28 (0.18%)	1.30 (0.81%)	0.91 (0.57%)	0.95 (0.59%)	0.84 (0.52%)
8		6	0.87 (0.54%)	0.32 (0.20%)	0.22 (0.14%)	0.38 (0.24%)	1.57 (0.98%)	1.08 (0.68%)	0.87 (0.54%)	0.50 (0.31%)
9		8	0.54 (0.34%)	0.43 (0.27%)	0.45 (0.28%)	0.49 (0.31%)	1.03 (0.64%)	1.47 (0.92%)	1.64 (1.02%)	0.54 (0.34%)
10		10	1.16 (0.72%)	1.01 (0.63%)	1.01 (0.63%)	0.69 (0.43%)	1.81 (1.13%)	1.90 (1.19%)	1.22 (0.76%)	1.63 (1.02%)
11	0.49	0	0.48 (0.30%)	0.83 (0.52%)	0.67 (0.42%)	0.27 (0.17%)	1.63 (1.02%)	1.59 (0.99%)	1.58 (0.99%)	1.67 (1.04%)
12		3	0.88 (0.55%)	0.88 (0.55%)	0.84 (0.52%)	0.52 (0.33%)	2.37 (1.48%)	2.04 (1.28%)	2.24 (1.40%)	1.00 (0.62%)
13		6	1.67 (1.04%)	1.09 (0.68%)	1.05 (0.66%)	0.76 (0.47%)	2.06 (1.29%)	2.12 (1.33%)	2.00 (1.25%)	1.87 (1.17%)
14		8	2.27 (1.42%)	1.44 (0.90%)	1.63 (1.02%)	0.92 (0.57%)	3.46 (2.16%)	1.91 (1.19%)	1.70 (1.06%)	1.35 (0.84%)
15		10	1.89 (1.18%)	0.49 (0.31%)	1.02 (0.64%)	0.70 (0.44%)	2.09 (1.31%)	1.74 (1.09%)	2.06 (1.29%)	0.88 (0.55%)

an average RMSE of 0.95 mm (0.59% of total length) and an average tip error of 1.49 mm (0.93% of total length). The maximum RMSE is 1.58 mm (0.99% of total length) and a maximum tip error is 4.19 mm (2.62% of total length) in all the tests.

For the cases 1–6 (single tendon actuated; Table 4), the average RMSE is 0.63 mm, 0.64 mm, 0.73 mm, 0.76 mm, 0.96 mm, and 1.07 mm, respectively. The average tip errors are 0.80 mm, 0.97 mm, 1.10 mm, 0.92 mm, 1.22 mm, and 1.49 mm, respectively. This reinforces the conclusion drawn in the first experiment that the RMSE increases as the tendon tension becomes larger. For the cases 7–10 (double tendons actuated) where the summation of the two tendon tensions are unchanged, the average RMSE is 1.16 mm, 1.14 mm, 1.17 mm, and 1.20 mm, respectively. The average tip errors are 1.87 mm, 1.88 mm, 1.75 mm, and 1.60 mm, respectively. This indicates that the accuracy of the proposed model is not affected by the number of tendon actuated. For the experiments with various depth of inserted Nitinol backbone (0 mm, 40 mm, 80 mm, and 120 mm), the average RMSE is 1.09 mm, 1.05 mm, 0.85 mm, and 0.78 mm, respectively. The average tip errors are 1.38 mm, 2.16 mm, 1.38 mm, and 1.03 mm, respectively. The RMSE drops as the depth of Nitinol tube increases, but the tip error increases as the Nitinol tube insertion depth increases from 0 mm to 40 mm and then decreases as the depth of Nitinol increases from 40 mm to 120 mm. This is potentially due to the model inaccuracy in the situation where short insertion depth and large tendon tension both exist. Since the stiffness of the Nitinol tube is high when the Nitinol tube insertion depth is short, interaction force between Nitinol tube and the inner wall of silicone body is intense. Thus, the Nitinol tube could press into the inner wall of the silicone body, and the concentric assumption of the model would fail.

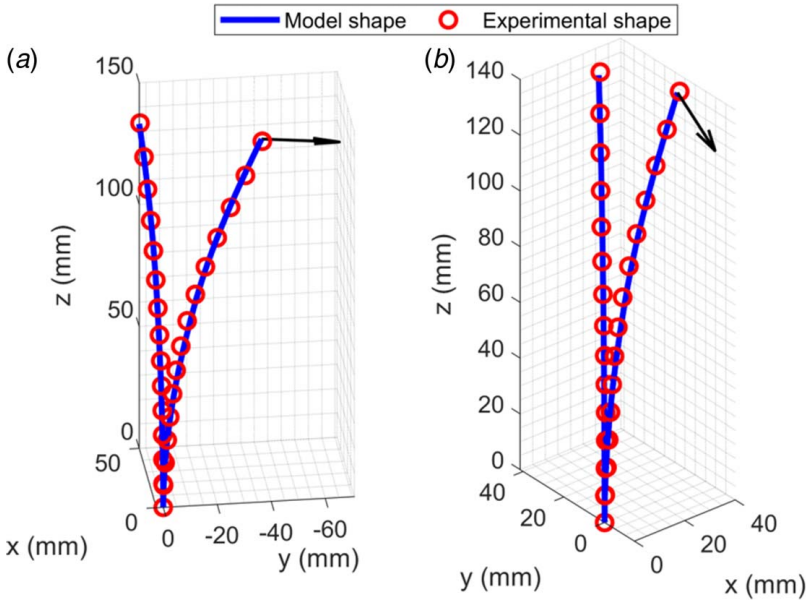

Fig. 7 Comparison of the modeling and experimental shape of the TDCT soft robot in 3D space. The black arrow indicates the external load: (*a*) The shape with no black arrow at the tip is subjected to single tendon force, and the other shape is subject to both the tendon force and external load and (*b*) The shape with no black arrow at the tip is subjected to double tendon forces, and the other shape is subject to both double tendon forces and external load

Table 4 Summary of multiple tendons actuation, out-of-plane external load experiment results

Tension (N)			RMSE (mm)				Tip error (mm)			
#1	#2	Load	$L = 0$ mm	$L = 40$ mm	$L = 80$ mm	$L = 120$ mm	$L = 0$ mm	$L = 40$ mm	$L = 80$ mm	$L = 120$ mm
0	0	Yes	0.30 (0.19%)	0.30 (0.19%)	0.31 (0.19%)	0.33 (0.21%)	0.96 (0.60%)	0.92 (0.57%)	0.73 (0.46%)	0.58 (0.36%)
2.94	0		0.61 (0.38%)	0.65 (0.41%)	0.43 (0.27%)	0.46 (0.29%)	1.59 (0.99%)	0.57 (0.36%)	0.60 (0.38%)	1.47 (0.92%)
3.92	0		0.92 (0.57%)	0.82 (0.51%)	0.52 (0.33%)	0.42 (0.26%)	1.53 (0.96%)	0.86 (0.54%)	1.13 (0.71%)	1.13 (0.71%)
4.91	0		0.93 (0.58%)	0.80 (0.50%)	0.64 (0.40%)	0.41 (0.26%)	1.51 (0.94%)	1.14 (0.71%)	0.42 (0.26%)	0.73 (0.46%)
5.89	0		1.05 (0.66%)	0.98 (0.61%)	0.83 (0.52%)	0.53 (0.33%)	1.81 (1.13%)	1.84 (1.15%)	0.59 (0.37%)	0.72 (0.45%)
6.87	0		1.26 (0.79%)	1.15 (0.72%)	0.79 (0.49%)	0.72 (0.45%)	1.44 (0.90%)	2.95 (1.84%)	0.98 (0.61%)	1.24 (0.78%)
2.94	5.89		1.12 (0.70%)	1.43 (0.89%)	0.95 (0.59%)	0.95 (0.59%)	1.54 (0.96%)	4.19 (2.62%)	2.22 (1.39%)	0.78 (0.49%)
3.92	4.91		1.34 (0.84%)	1.39 (0.87%)	0.97 (0.61%)	0.84 (0.52%)	1.30 (0.81%)	4.39 (2.74%)	1.93 (1.21%)	1.02 (0.64%)
4.91	3.92		1.58 (0.99%)	1.33 (0.83%)	0.96 (0.60%)	0.87 (0.54%)	1.66 (1.04%)	3.15 (1.97%)	1.86 (1.16%)	0.80 (0.50%)
5.89	2.94		1.45 (0.91%)	1.39 (0.87%)	1.01 (0.63%)	0.92 (0.57%)	1.29 (0.81%)	3.42 (2.14%)	1.43 (0.89%)	0.68 (0.43%)
0	0	No	0.90 (0.56%)	0.98 (0.61%)	0.97 (0.61%)	0.91 (0.57%)	1.23 (0.77%)	3.20 (2.00%)	3.59 (2.24%)	2.79 (1.74%)
2.94	0		0.83 (0.52%)	0.76 (0.47%)	0.51 (0.32%)	0.87 (0.54%)	1.17 (0.73%)	0.86 (0.54%)	0.65 (0.41%)	0.88 (0.55%)
3.92	0		0.99 (0.62%)	0.93 (0.58%)	0.58 (0.36%)	0.67 (0.42%)	1.23 (0.77%)	0.96 (0.60%)	0.93 (0.58%)	1.04 (0.65%)
4.91	0		0.99 (0.62%)	0.92 (0.57%)	0.71 (0.44%)	0.73 (0.46%)	1.32 (0.83%)	0.91 (0.57%)	0.59 (0.37%)	0.75 (0.47%)
5.89	0		1.15 (0.72%)	1.09 (0.68%)	1.29 (0.81%)	0.73 (0.46%)	1.27 (0.79%)	1.42 (0.89%)	1.38 (0.86%)	0.72 (0.45%)
6.87	0		1.22 (0.76%)	1.15 (0.72%)	1.29 (0.81%)	0.95 (0.59%)	1.45 (0.91%)	1.92 (1.20%)	1.06 (0.66%)	0.91 (0.57%)
2.94	5.89		1.36 (0.85%)	1.30 (0.81%)	1.09 (0.68%)	1.11 (0.69%)	1.27 (0.79%)	2.37 (1.48%)	1.64 (1.02%)	0.97 (0.61%)
3.92	4.91		1.29 (0.81%)	1.22 (0.76%)	0.97 (0.61%)	1.08 (0.68%)	0.83 (0.52%)	2.53 (1.58%)	2.00 (1.25%)	1.05 (0.66%)
4.91	3.92		1.30 (0.81%)	1.23 (0.77%)	1.03 (0.64%)	1.09 (0.68%)	1.29 (0.81%)	3.26 (2.04%)	1.32 (0.83%)	0.67 (0.42%)
5.89	2.94		1.30 (0.81%)	1.23 (0.77%)	1.14 (0.71%)	1.15 (0.72%)	1.24 (0.78%)	2.39 (1.49%)	1.81 (1.13%)	0.57 (0.36%)

4 Kinematics and Stiffness Analysis of TDCT Soft Robot

This section discusses the simulation results of Nitinol backbone on the TDCT soft robot from the aspects of tip pose and robot compliance. Note that compliance is considered as the opposite of stiffness. According to the prior work of continuum robot modeling [49], we use compliance as the performance index to evaluate the TDCT soft robot stiffness.

4.1 TDCT Soft Robot Kinematics Characterization. This section aims to investigate the kinematics of TDCT soft robot in terms of tip workspace, position, and orientation, subject to the variation of Nitinol backbone insertion depths and tendon tensions. Note that in this study, we only actuated tendon 1 to create in-plane bending (see Fig. 2 for tendon location) because the actuation of multiple tendons can result in a planar deformation as that of single tendon input [50].

To systematically analyze the robot tip pose, we conduct a series of simulation studies where tendon force increases from 0 N to 10 N with 1 N per increment, while the Nitinol backbone insertion depth increases from 0 mm to 150 mm with 10 mm per increment. The robot tip position is presented in z_o–y_o plane, and the tip orientation is defined as the tangent angle at the tip (θ_{tip} in Fig. 8(*a*)). The workspace of the TDCT soft robot, as shown in Fig. 8(*b*), is enhanced by the insertion of the Nitinol backbone, allowing the tip to reach a larger area compared to a standard tendon-driven soft robot whose tip can only move along a curve. This is intuitive to understand since the increased workspace is caused by the additional Nitinol backbone insertion DoF.

The details of the soft robot tip pose changes (positions and orientations) with respect to Nitinol backbone insertion depth are shown in Fig. 9. As the figure shows, the magnitude of the gradient of z_{tip} and y_{tip} becomes smaller as the Nitinol backbone insertion depth increases (Figs. 9(*a*) and 9(*b*)), indicating that the effect of Nitinol backbone on the tip position becomes smaller as the insertion depth increases. However, Fig. 9(*c*) shows that the TDCT soft robot orientation angle gradually reduces with the insertion of the Nitinol backbone since it tends to straighten the robot system.

4.2 TDCT Soft Robot Stiffness Analysis. The mechanics modeling has shown that the TDCT soft robot stiffness can be changed with the presence of the Nitinol backbone. This section will systematically investigate the Nitinol backbone's effect on

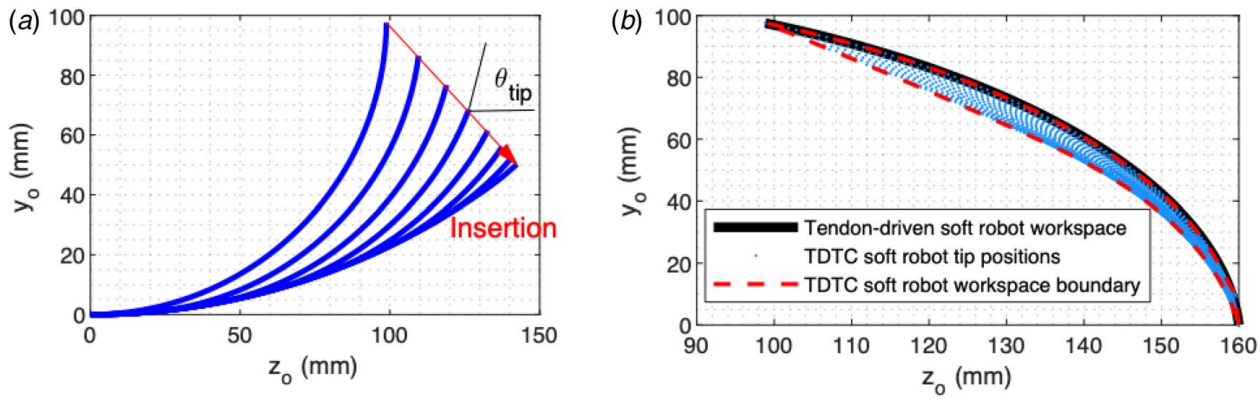

Fig. 8 (*a*) TDCT soft robot deformation caused by the varying Nitinol backbone insertions. The arrow indicates the direction of soft robot tip motion while inserting the Nitinol backbone and (*b*) The workspace of the TDCT soft robot with/without the Nitinol backbone insertion DoF. The Nitinol backbone enlarges the workspace of the TDCT soft robot from a curve (solid curve) to an area (dashed line).

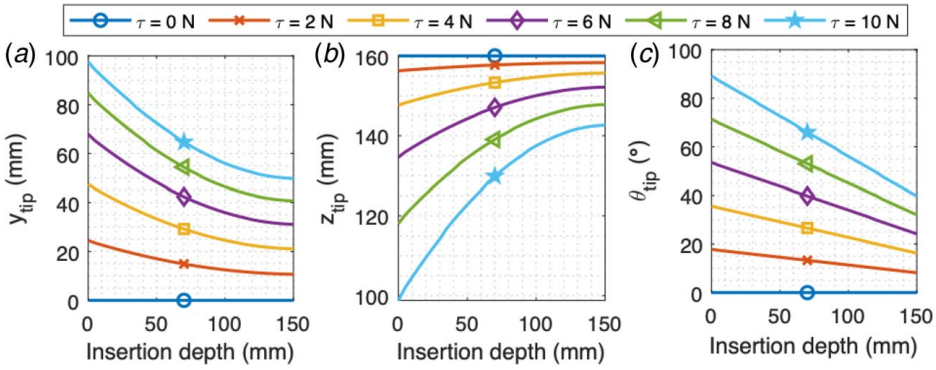

Fig. 9 Soft robot tip pose with various insertion depths of Nitinol backbone. In all cases, tip load is set to zero, tendon tension τ is increased from 0 N to 10 N with 1 N per increment, and the Nitinol backbone insertion depth increases from 0 mm to 150 mm with 10 mm per increment: (*a*) and (*b*) The tip position (z_{tip} and y_{tip}) changes and (*c*) Describes the orientation θ_{tip} changes of the soft robot. Overall, the insertion of Nitinol backbone can significantly change the TDCT soft robot tip pose

the robot stiffness at the tip. In this paper, compliance ellipsoid (CE) [49] is utilized to visualize the relationship between a small external force applied on the tip and the induced tip position change, which can be written as

$$\mathrm{CE} = \{\delta \boldsymbol{p}(L) : \|\delta \boldsymbol{f}_{\mathrm{tip}}\| = 1\} \tag{40}$$

where $\boldsymbol{f}_{\mathrm{tip}}$ is the force expressed in global coordinate at the tip. Note that the principle axes and the magnitudes of CE can be obtained when the compliance matrix (CM) is obtained, which is defined as

$$\mathrm{CM} = \frac{\partial \boldsymbol{p}(L)}{\partial \boldsymbol{f}_{\mathrm{tip}}} \tag{41}$$

The CM is a 3 by 3 symmetric matrix, which has eigenvalues λ_1, λ_2, λ_3, and corresponding eigenvectors $\boldsymbol{\mu}_1, \boldsymbol{\mu}_2, \boldsymbol{\mu}_3$. Using the first-order approximation, the relationship between $\delta \boldsymbol{p}(L)$ and $\delta \boldsymbol{f}_{\mathrm{tip}}$ can be written as

$$\delta \boldsymbol{p}(L) = \mathrm{CM}\ \delta \boldsymbol{f}_{\mathrm{tip}} \tag{42}$$

which can be substituted into the condition in (40) and becomes

$$\delta \boldsymbol{p}(L)^T (\mathrm{CM}\ \mathrm{CM}^T)^{-1} \delta \boldsymbol{p}(L) = 1 \tag{43}$$

which indicates that the principle axes of the CE are $\boldsymbol{\mu}_1, \boldsymbol{\mu}_2, \boldsymbol{\mu}_3$ with magnitudes λ_1, λ_2, λ_3, respectively.

In this paper, CM is computed numerically by finite difference method as indicated in (41), and then the dimension of CE can be obtained. Figure 10 shows an example of the CE projected in μ_2–μ_3 plane with different Nitinol backbone insertion depth, indicating that the insertion of Nitinol backbone could lead to the reduced tip compliance of the TDCT soft robot, also known as the increased stiffness. Note that this result was obtained with a constant tendon tension such that only the Nitinol backbone effect on the robot compliance is considered.

We further characterized the TDCT soft robot compliance caused by both tendon tension and Nitinol backbone insertion depth. In these simulations, the insertion depth of the Nitinol backbone was increased from 0 mm to 150 mm with 10 mm increments, and the tendon tension was increased from 0 N to 8 N with 2 N increments. Figure 11 shows that the values of λ_2 and λ_3 are two orders of magnitude larger than the value of λ_1, indicating that the dimension of CE is mostly determined by λ_2 and λ_3. Moreover, the TDCT soft robot compliance could be significantly reduced due to Nitinol backbone insertion, but the tendon tension effect on the compliance is minimal or negligible. For example, the value of λ_2 is decreased from 203.5 mm/N to 86.1 mm/N in Fig. 11 when the Nitinol backbone gradually increased from 0 mm to 150 mm, showing a 57.7% reduction of compliance in the major axis of the CE. However, the values of λ_2 or λ_3 for various tendon tensions in Fig. 11 are close to each other, showing that the tendon tension has an insignificant contribution to the TDCT soft robot tip compliance.

5 Potential Applications

We have demonstrated the enhanced kinematics and stiffness of the proposed TDCT soft robot in the prior sections. In this section, we explore two potential applications of the proposed design in the practical applications.

5.1 Object Manipulation. This section aims to explore the application of the TDCT soft robot for object manipulation. Figure 12 presents four scenarios of the TDCT soft robot deformation due to the Nitinol backbone insertion variation to manipulate an 50 g external object. The Nitinol backbone tends to straighten the TDCT soft robot by making the overall structure stiffer, which leads to the external object motion (see Fig. 12 for the object motion). This motion is analogous to the robotic pick-place task,

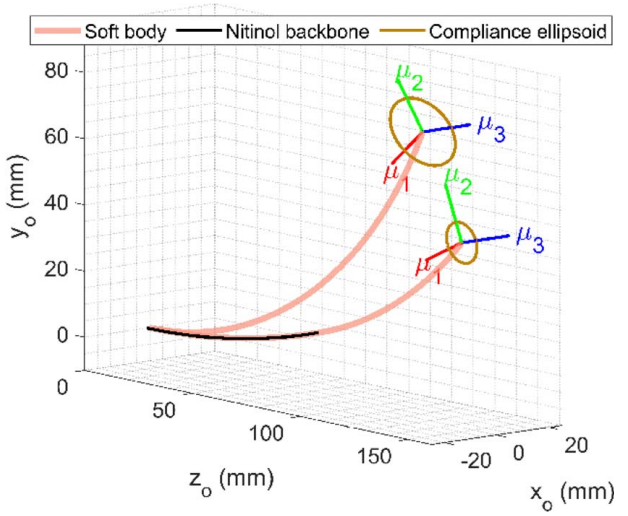

Fig. 10 CE projected in μ_2–μ_3 plane with various Nitinol backbone insertion and constant tendon tension, where μ_1, μ_2, μ_3 are eigenvectors of CM. The dimension of the CE becomes smaller with Nitinol backbone inserted, indicating the stiffness of the TDCT soft robot tip is enhanced.

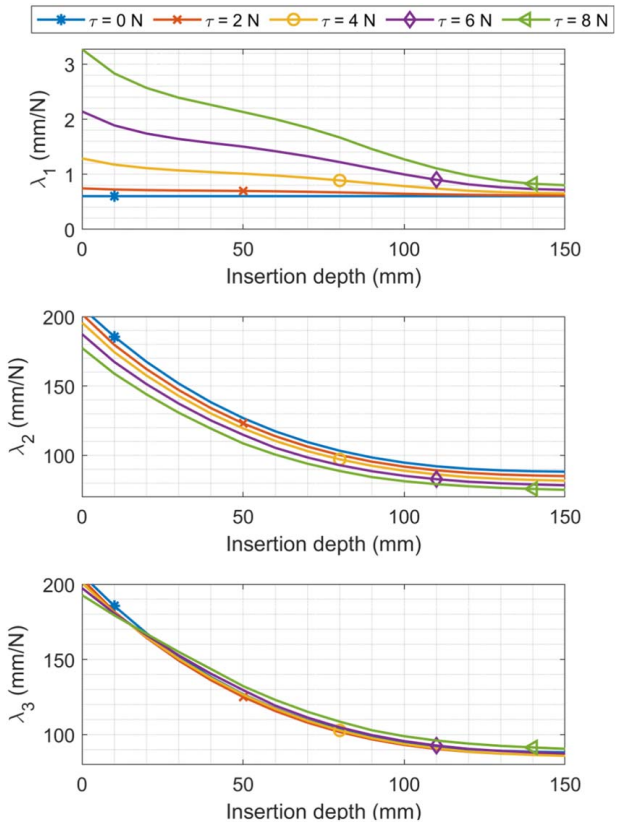

Fig. 11 The relationship between eigen value λ and Nitinol backbone insertion depth with various tendon tensions. The dimension of CE significantly decreases as the insertion depth increases. This shows that the stiffness of the TDCT robot tip is enhanced caused by the Nitinol backbone.

where the TDCT soft robot moves the object from the initial position (Fig. 12(*a*), without Nitinol backbone insertion) to the desired position (Fig. 12(*d*), with Nitinol backbone insertion) by simply inserting the backbone. Thus, the proposed TDCT soft robot demonstrates improved stiffness and shows its advantage in object manipulation by simply inserting the Nitinol backbone.

Simulation studies in Fig. 13(*a*) indicate that maximum tip displacement in y_o direction ($\Delta y_{\max}$) is a function of Nitinol backbone insertion depth. Note that the simulations were performed with a constant 10 N tendon force. For constant tip load and tendon tension, $\Delta y_{\max}$ is defined as

$$\Delta y_{\max} = y_{\text{tip, max}} - y_{\text{tip},0} \tag{44}$$

where $y_{\text{tip, max}}$ is the maximum value of y_{tip}, y_{tip}, 0 is the initial value of y_{tip} without Nitinol backbone insertion. Instead of inserting the Nitinol backbone with the maximum depth L, Fig. 13(*a*) shows that there is an optimal insertion depth for a given external load such that the maximum tip displacement $\Delta y_{\max}$ can be obtained. The existence of the optimal insertion depth implies the trade-off between stiffness and compliance. If no Nitinol backbone is inserted, the soft robot will become too compliant to hold the load at the tip. If Nitinol backbone is fully inserted, the soft robot will become too stiff for the tendon to actuate the robot. These two extreme cases will hinder the soft robot to reach the highest position. For example, the TDCT soft robot tip could pick an external load of 50 g and move it towards the largest y_{tip} with 70 mm insertion depth (shorter than the TDCT soft robot length L). Same conclusion could be drawn when tendon tension equals to 5 N as shown in Fig. 13(*b*).

Another noteworthy feature of the TDCT soft robot for object manipulation is that it can increase the tip load capacity. Figure 14 shows the simulation result to move a object to the same height ($y_0 = 0$ mm) with the various tendon tension (6–10 N). Tendon-driven soft robot without Nitinol backbone can only move 7.20 g, 13.74 g, 20.35 g, 27.04 g, and 33.82 g load to the desired height with tendon tension 6 N, 7 N, 8 N, 9 N, and 10 N, respectively. However, these load capacities can be increased to 18.44 g, 26.15 g, 33.97 g, 41.91 g, and 49.98 g with 70 mm Nitinol backbone inserted, which increases 156.11%, 90.32%, 66.93%, 54.96%, and 47.78% of the load capacity of the tendon-drive soft robot with no Nitinol backbone. Notice that if the Nitinol insertion depth is larger than 70 mm, the load capacity will decrease. This is caused by the trade-off between the Nitinol depth and the tendon tension. The excessive insertion of Nitinol tube increases the stiffness of the TDCT soft robot, which reduces the effect of tendon tension on TDCT soft robot deformations.

5.2 Soft Robotic Laparoscopy for Photodynamic Therapy.

Laparoscopic instruments are typically fabricated with rigid materials and used in a variety of abdominal procedures [51]. Due to the limited DoF of the rigid tubes, surgeons have to tilt the laparoscopic instrument around the entry points in order to reach a large

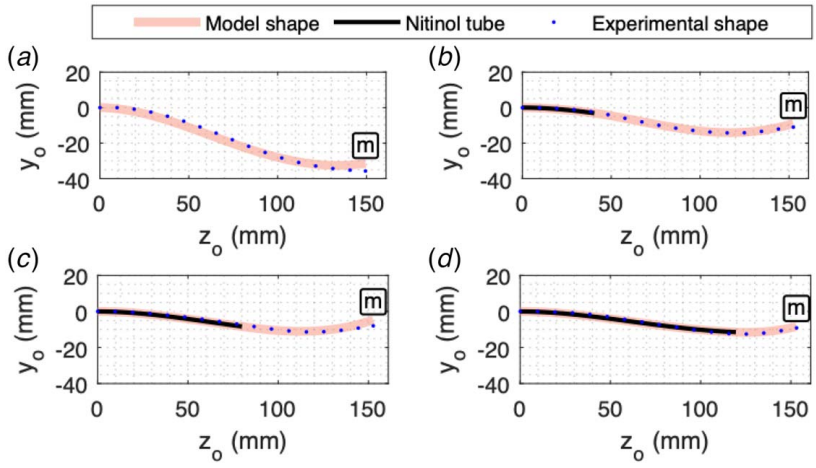

Fig. 12 Experimental study of object manipulation with various Nitinol backbone insertion depth and constant tendon tension. The TDCT soft robot is actuated by 10 N tendon tension to lift a 50 g object with (*a*) 0 mm, (*b*) 40 mm, (*c*) 80 mm, and (*d*) 120 mm Nitinol backbone insertion depth, respectively.

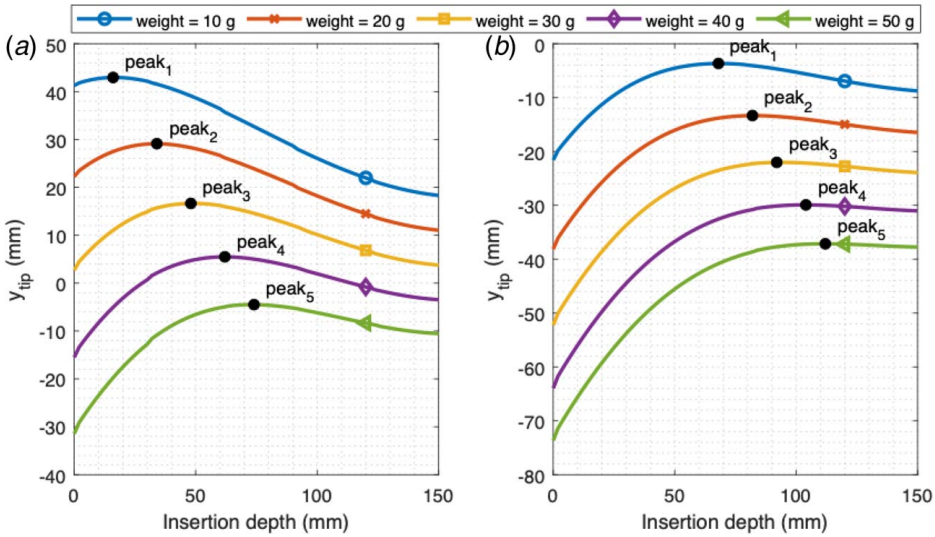

Fig. 13 Simulation studies of detailed Nitinol backbone tip position y_{tip} for various object weights and Nitinol backbone insertion depth. The peaks $y_{tip,\,max}$ of each curve are highlighted with black dot marker. The tendon tension of (*a*) is 10 N, and the tendon tension of (*b*) is 5 N, respectively.

workspace within the abdomen. However, this tilting motion has certain limitations in the practical scenarios, including the limited capability to reach a target at the deeper region within the confined abdomen, such as the pancreas that is surrounded by bile duct, duodenum, transverse colon, and part of the stomach. Recently, we proposed a tendon-driven soft robotic laparoscope enabled photodynamic therapy for pancreatic cancer treatment (see Fig. 15 for the schematic diagram of the soft robotic laparoscope [52]).

During the pancreatic cancer photodynamic therapy, the soft robotic laparoscope will carry a diffusing fiber and face to the target at the desired orientation such that the photosensitizer could absorb sufficient 690 nm laser light energy to destroy the cancerous cell. Compared to the tendon-driven soft robotic laparoscope [52], the TDCT soft robot design developed in this study has an additional backbone insertion DoF, which could significantly enhance the photodynamic therapy (PDT) treatment performance. Note that the additional DoF also offers redundant resolution in terms of the in-plane soft robot tip orientation control, which could be highly beneficial in the practical scenarios when the soft robot needs to reach the desired location and orientation simultaneously.

We experimentally validated the TDCT soft robot orientation control performance by integrating a micro-camera (outer diameter: 1.4 mm, minnieScope-XS PN: ENA-10005-AS, Enable Inc., Redwood City, CA) with the robot body. Then the camera extrinsic orientation parameters under various Nitinol backbone insertion inputs are obtained using MATLAB camera calibration toolbox. Error is defined as the difference between the desired orientation

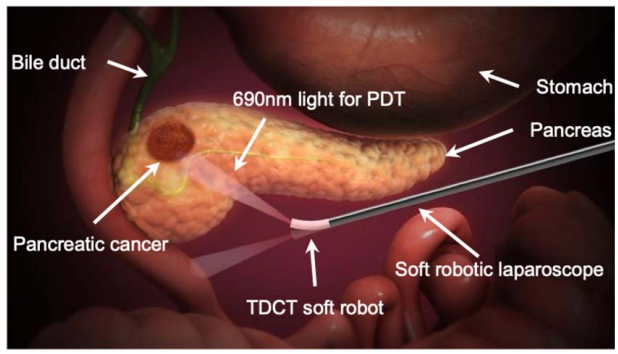

Fig. 15 Soft robotic laparoscope for pancreatic cancer treatment via PDT

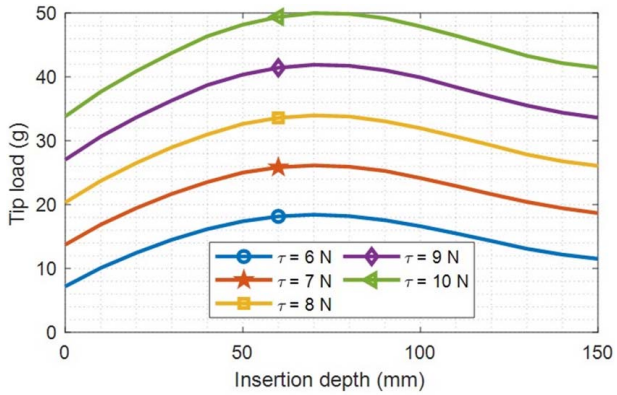

Fig. 14 Simulation result of the tip load capacity change with respect to the insertion depth of Nitinol tube

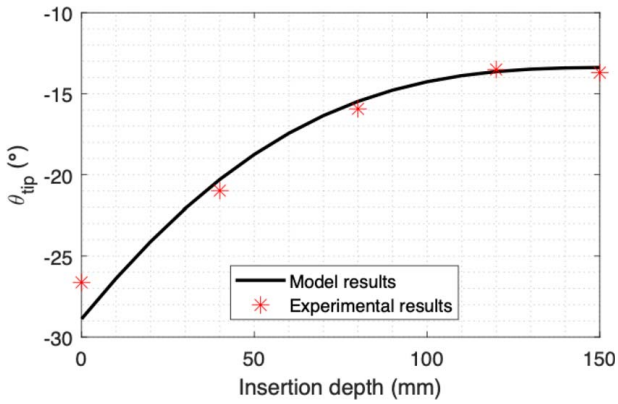

Fig. 16 Experimental validations of the tip orientation θ_{tip}. The red asterisks are experimental results calculated from micro-camera.

angle and the actual orientation angle. The experimental results (Fig. 16) indicate that the TDCT soft robotic laparoscope could achieve an orientation error of 0.77 ± 0.85 deg, which demonstrates the improvement compared to our prior results 1.5 ± 1.1 deg [52].

6 Conclusion

This paper presented a novel stiffness modulation method for soft robots based on a TDCT design. The mechanics modeling of the TDCT soft robot was achieved through the Cosserat rod theory. The proposed model was validated by two experiments: (1) single tendon actuation with applying loads align with the bending plane and (2) multiple tendons actuated with applying loads not align with the bending plane. The result of the first experiment showed a maximum RMSE of 2.27 mm (1.42% of total length) and a maximum tip error of 3.46 mm (2.16% of total length). The average RMSE and tip error were 0.75 mm (0.47% of total length) and 1.48 mm (0.92% of total length), respectively. The result of the second experiment showed a maximum RMSE of 1.58 mm (0.99% of total length) and a maximum tip error of 4.19 mm (2.62% of total length). The average RMSE and tip error were 0.95 mm (0.59% of total length) and 1.49 mm (0.93% of total length), respectively. These experiments validated the accuracy of the proposed model to predict the shape of the TDCT soft robot. The derived kinematics/mechanics model was then applied to perform kinematics and stiffness analysis of the TDCT soft robot. The kinematics analysis showed that the tip pose and the workspace of the TDCT soft robot were enhanced compared to the conventional tendon-driven soft robot. Stiffness analysis showed that the tip compliance of the TDCT soft robot can be reduced by 57.7%. Two potential applications of the proposed TDCT robot were presented and analyzed. For object manipulation, it was shown that the TDCT soft robot is capable of enhancing the moving position as well as the tip load capacity with an optimal backbone insertion depth. The orientation control experiment demonstrated the obvious improvement of accuracy for soft robot-based photodynamic therapy.

Future work will focus on the contact analysis [53] and dynamic control [54] of the proposed TDCT robot. Additionally, we will explore other clinical applications that cannot be achieved with the conventional tools, such as atrial fibrillation ablation therapy [55].

Acknowledgment

This work was supported by Georgia Tech IRIM and GTRI seed grant, Georgia Tech EVPR seed grant, and National Science Foundation grant IIS-1718755.

Conflict of Interest

There are no conflicts of interest.

Data Availability Statement

The authors attest that all data for this study are included in the paper.

References

[1] Tse, Z. T. H., Chen, Y., Hovet, S., Ren, H., Cleary, K., Xu, S., Wood, B., and Monfaredi, R., 2018, "Soft Robotics in Medical Applications," J. Med. Rob. Res., **3**(3–4), p. 1841006.

[2] Galloway, K. C., Chen, Y., Templeton, E., Rife, B., Godage, I. S., and Barth, E. J., 2019, "Fiber Optic Shape Sensing for Soft Robotics," Soft Rob., **6**(5), pp. 671–684.

[3] Manti, M., Cacucciolo, V., and Cianchetti, M., 2016, "Stiffening in Soft Robotics: A Review of the State of the Art," IEEE Rob. Autom. Mag., **23**(3), pp. 93–106.

[4] Langer, M., Amanov, E., and Burgner-Kahrs, J., 2018, "Stiffening Sheaths for Continuum Robots," Soft Rob., **5**(3), pp. 291–303.

[5] Yang, Y., Li, Y., and Chen, Y., 2018, "Principles and Methods for Stiffness Modulation in Soft Robot Design and Development," Bio-Des. Manuf., **1**(1), pp. 14–25.

[6] Al-Rubaiai, M., Pinto, T., Qian, C., and Tan, X., 2019, "Soft Actuators With Stiffness and Shape Modulation Using 3d-Printed Conductive Polylactic Acid Material," Soft Rob., **6**(3), pp. 318–332.

[7] Zhang, Y. F., Zhang, N. B., Hingorani, H., Ding, N. Y., Wang, D., Yuan, C., Zhang, B., Gu, G. Y., and Ge, Q., 2019, "Fast-Response, Stiffness-Tunable Soft Actuator by Hybrid Multimaterial 3d Printing," Adv. Funct. Mater., **29**(15), p. 9.

[8] Yang, Y., Chen, Y., Li, Y., Chen, M. Z., and Wei, Y., 2017, "Bioinspired Robotic Fingers Based on Pneumatic Actuator and 3d Printing of Smart Material," Soft Rob., **4**(2), pp. 147–162.

[9] Yang, Y., Chen, Y., Li, Y., Wang, Z., and Li, Y., 2017, "Novel Variable-Stiffness Robotic Fingers With Built-In Position Feedback," Soft Rob., **4**(4), pp. 338–352.

[10] Firouzeh, A., Salerno, M., and Paik, J., 2017, "Stiffness Control With Shape Memory Polymer in Underactuated Robotic Origamis," IEEE Trans. Rob., **33**(4), pp. 765–777.

[11] Wang, W., and Ahn, S.-H., 2017, "Shape Memory Alloy-Based Soft Gripper With Variable Stiffness for Compliant and Effective Grasping," Soft Rob., **4**(4), pp. 379–389.

[12] Yuen, M. C., Bilodeau, R. A., and Kramer, R. K., 2016, "Active Variable Stiffness Fibers for Multifunctional Robotic Fabrics," IEEE Rob. Autom. Lett., **1**(2), pp. 708–715.

[13] Wang, J. C., Wang, S. X., Li, J. H., Ren, X. Y., and Briggs, R. M., 2018, "Development of a Novel Robotic Platform With Controllable Stiffness Manipulation Arms for Laparoendoscopic Single-Site Surgery (LESS)," Int. J. Med. Rob. Comput. Assist. Surg., **14**(1), p. 16.

[14] Schubert, B. E., and Floreano, D., 2013, "Variable Stiffness Material Based on Rigid Low-Melting-Point-Alloy Microstructures Embedded in Soft Poly (Dimethylsiloxane)(PDMS)," RSC Adv., **3**(46), pp. 24671–24679.

[15] Shintake, J., Schubert, B., Rosset, S., Shea, H., and Floreano, D., 2015, "Variable Stiffness Actuator for Soft Robotics Using Dielectric Elastomer and Low-Melting-Point Alloy," 2015 IEEE/RSJ International Conference on Intelligent Robots and Systems (IROS), Hamburg, Germany, Dec. 17, IEEE, pp. 1097–1102.

[16] Hao, Y., Wang, T., and Wen, L., 2017, "A Programmable Mechanical Freedom and Variable Stiffness Soft Actuator With Low Melting Point Alloy," International Conference on Intelligent Robotics and Applications, Wuhan, China, Aug. 6, Springer, pp. 151–161.

[17] Nakai, H., Kuniyoshi, Y., Inaba, M., and Inoue, H., 2002, "Metamorphic Robot Made of Low Melting Point Alloy," IEEE/RSJ International Conference on Intelligent Robots and Systems, Lausanne, Switzerland, Dec. 10, Vol. 2, IEEE, pp. 2025–2030.

[18] Cheng, N. G., Gopinath, A., Wang, L., Iagnemma, K., and Hosoi, A. E., 2014, "Thermally Tunable, Self-Healing Composites for Soft Robotic Applications," Macromol. Mater. Eng., **299**(11), pp. 1279–1284.

[19] Pettersson, A., Davis, S., Gray, J. O., Dodd, T. J., and Ohlsson, T., 2010, "Design of a Magnetorheological Robot Gripper for Handling of Delicate Food Products With Varying Shapes," J. Food Eng., **98**(3), pp. 332–338.

[20] Majidi, C., and Wood, R. J., 2010, "Tunable Elastic Stiffness With Microconfined Magnetorheological Domains at Low Magnetic Field," Appl. Phys. Lett., **97**(16), p. 164104.

[21] Tonazzini, A., Sadeghi, A., and Mazzolai, B., 2016, "Electrorheological Valves for Flexible Fluidic Actuators," Soft Rob., **3**(1), pp. 34–41.

[22] Song, B.-K., Yoon, J.-Y., Hong, S.-W., and Choi, S.-B., 2020, "Field-Dependent Stiffness of a Soft Structure Fabricated From Magnetic-Responsive Materials: Magnetorheological Elastomer and Fluid," Materials, **13**(4), p. 953.

[23] Wei, Y., Chen, Y., Ren, T., Chen, Q., Yan, C., Yang, Y., and Li, Y., 2016, "A Novel, Variable Stiffness Robotic Gripper Based on Integrated Soft Actuating and Particle Jamming," Soft Rob., **3**(3), pp. 134–143.

[24] Steltz, E., Mozeika, A., Rodenberg, N., Brown, E., and Jaeger, H. M., 2009, "JSEL: Jamming Skin Enabled Locomotion," 2009 IEEE/RSJ International Conference on Intelligent Robots and Systems, St. Louis, MO, Dec. 15, IEEE, pp. 5672–5677.

[25] Li, Y., Chen, Y., Yang, Y., and Wei, Y., 2017, "Passive Particle Jamming and Its Stiffening of Soft Robotic Grippers," IEEE Trans. Rob., **33**(2), pp. 446–455.

[26] Kim, Y.-J., Cheng, S., Kim, S., and Iagnemma, K., 2013, "A Novel Layer Jamming Mechanism With Tunable Stiffness Capability for Minimally Invasive Surgery," IEEE Trans. Rob., **29**(4), pp. 1031–1042.

[27] Wall, V., Deimel, R., and Brock, O., 2015, "Selective Stiffening of Soft Actuators Based on Jamming," 2015 IEEE International Conference on Robotics and Automation (ICRA), IEEE, pp. 252–257.

[28] Robertson, M. A., and Paik, J., 2017, "New Soft Robots Really Suck: Vacuum-Powered Systems Empower Diverse Capabilities," Sci. Rob., **2**(9), p. eaan6357.

[29] Jiang, A., Ranzani, T., Gerboni, G., Lekstutyte, L., Althoefer, K., Dasgupta, P., and Nanayakkara, T., 2014, "Robotic Granular Jamming: Does the Membrane Matter?" Soft Rob., **1**(3), pp. 192–201.

[30] English, C., and Russell, D., 1999, "Implementation of Variable Joint Stiffness Through Antagonistic Actuation Using Rolamite Springs," Mech. Mach. Theory, **34**(1), pp. 27–40.

[31] Ansari, Y., Manti, M., Falotico, E., Cianchetti, M., and Laschi, C., 2017, "Multiobjective Optimization for Stiffness and Position Control in a Soft Robot Arm Module," IEEE Rob. Autom. Lett., **3**(1), pp. 108–115.

[32] Fathi, J., Vrielink, T. J. O., Runciman, M. S., and Mylonas, G. P., 2019, "A Deployable Soft Robotic Arm With Stiffness Modulation for Assistive Living

Applications," 2019 International Conference on Robotics and Automation (ICRA), Montreal, QC, Canada, Aug. 12, IEEE, pp. 1479–1485.
[33] Stilli, A., Wurdemann, H. A., and Althoefer, K., 2014, "Shrinkable, Stiffness-Controllable Soft Manipulator Based on a Bio-Inspired Antagonistic Actuation Principle," 2014 IEEE/RSJ International Conference on Intelligent Robots and Systems, Chicago, IL, Nov. 6, IEEE, pp. 2476–2481.
[34] Dupont, P. E., Lock, J., Itkowitz, B., and Butler, E., 2009, "Design and Control of Concentric-Tube Robots," IEEE Trans. Rob., **26**(2), pp. 209–225.
[35] Rucker, D. C., Jones, B. A., and Webster III, R. J., 2010, "A Geometrically Exact Model for Externally Loaded Concentric-Tube Continuum Robots," IEEE Trans. Rob., **26**(5), p. 769.
[36] Godage, I. S., Medrano-Cerda, G. A., Branson, D. T., Guglielmino, E., and Caldwell, D. G., 2016, "Dynamics for Variable Length Multisection Continuum Arms," Int. J. Rob. Res., **35**(6), pp. 695–722.
[37] Webster III, R. J., and Jones, B. A., 2010, "Design and Kinematic Modeling of Constant Curvature Continuum Robots: A Review," Int. J. Rob. Res., **29**(13), pp. 1661–1683.
[38] Schlagenhauf, C., Bauer, D., Chang, K.-H., King, J. P., Moro, D., Coros, S., and Pollard, N., 2018, "Control of Tendon-Driven Soft Foam Robot Hands," 2018 IEEE-RAS 18th International Conference on Humanoid Robots (Humanoids), Beijing, China, Nov. 9, IEEE, pp. 1–7.
[39] Trivedi, D., Lotfi, A., and Rahn, C. D., 2008, "Geometrically Exact Models for Soft Robotic Manipulators," IEEE Trans. Rob., **24**(4), pp. 773–780.
[40] Chen, Y., Wang, L., Galloway, K., Godage, I., Simaan, N., and Barth, E., 2020, "Modal-Based Kinematics and Contact Detection of Soft Robots," Soft Rob., **8**(3), pp. 298–309.
[41] Rucker, D. C., and Webster, R. J., 2010, "Mechanics of Continuum Robots With External Loading and General Tendon Routing," ISER, Naples, Italy, Dec. 10.
[42] Janabi-Sharifi, F., Jalali, A., and Walker, I. D., 2021, "Cosserat Rod-Based Dynamic Modeling of Tendon-Driven Continuum Robots: A Tutorial," IEEE Access, **9**, pp. 68703–68719.
[43] Till, J., Aloi, V., Riojas, K. E., Anderson, P. L., Webster III, R. J., and Rucker, C., 2020, "A Dynamic Model for Concentric Tube Robots," IEEE Trans. Rob., **36**(6), pp. 1704–1718.
[44] Xu, K., and Simaan, N., 2010, "Analytic Formulation for Kinematics, Statics, and Shape Restoration of Multibackbone Continuum Robots Via Elliptic Integrals," ASME J. Mech. Rob., **2**(1), p. 011006.
[45] Zwillinger, D., and Dobrushkin, V., 1998, *Handbook of Differential Equations*, Chapman and Hall/CRC, Boca Raton, FL.
[46] Burgner-Kahrs, J., Rucker, D. C., and Choset, H., 2015, "Continuum Robots for Medical Applications: A Survey," IEEE Trans. Rob., **31**(6), pp. 1261–1280.
[47] Rucker, D. C., and Webster, R. J., 2011, "Computing Jacobians and Compliance Matrices for Externally Loaded Continuum Robots," 2011 IEEE International Conference on Robotics and Automation, Shanghai, China, May 13, IEEE, pp. 945–950.
[48] Duriez, C., Coevoet, E., Largilliere, F., Morales-Bieze, T., Zhang, Z., Sanz-Lopez, M., Carrez, B., Marchal, D., Goury, O., and Dequidt, J., 2016, "Framework for Online Simulation of Soft Robots With Optimization-Based Inverse Model," 2016 IEEE International Conference on Simulation, Modeling, and Programming for Autonomous Robots (SIMPAR), San Francisco, CA, Dec. 16, IEEE, pp. 111–118.
[49] Gravagne, I. A., and Walker, I. D., 2002, "Manipulability, Force, and Compliance Analysis for Planar Continuum Manipulators," IEEE Trans. Rob. Autom., **18**(3), pp. 263–273.
[50] Walker, I., and Gravagne, I., 2002, "Design, Analysis and Experimentation: The Fundamentals of Continuum Robotic Manipulators," Clemson University ProQuest Dissertations Publishing, 3057195.
[51] Sauerland, S., Agresta, F., Bergamaschi, R., Borzellino, G., Budzynski, A., Champault, G., Fingerhut, A., Isla, A., Johansson, M., Lundorff, P., and Navez, B., 2006, "Laparoscopy for Abdominal Emergencies," Surg. Endosc. Other Intervent. Tech., **20**(1), pp. 14–29.
[52] Li, Y., Liu, Y., Yamazaki, K., Bai, M., and Chen, Y., 2021, "Development of a Soft Robot-Based Photodynamic Therapy for Pancreatic Cancer," IEEE/ASME Trans. Mechatron., **26**(6), pp. 2977–2985.
[53] Chen, Y., Wang, L., Galloway, K., Godage, I., Simaan, N., and Barth, E., 2021, "Modal-Based Kinematics and Contact Detection of Soft Robots," Soft Rob., **8**(3), pp. 298–309.
[54] Azizkhani, M., Godage, I. S., and Chen, Y., 2022, "Dynamic Control of Soft Robotic Arm: A Simulation Study," IEEE Rob. Autom. Lett., **7**(2), pp. 3584–3591.
[55] Alipour, A., Meyer, E. S., Dumoulin, C. L., Watkins, R. D., Elahi, H., Loew, W., Schweitzer, J., Olson, G., Chen, Y., Tao, S., and Guttman, M., and 2019, "MRI Conditional Actively Tracked Metallic Electrophysiology Catheters and Guidewires With Miniature Tethered Radio-Frequency Traps: Theory, Design, and Validation," IEEE Trans. Biomed. Eng., **67**(6), pp. 1616–1627.